International Journal of ISSI, Vol. 22(2025), No. 2, pp. 63-76

Online ISSN: 2981-0396 Print ISSN: 2981-0388

International Journal of Iron & Steel Society of Iran

Journal Homepage: https://journal.issiran.com/

Research Article

Investigation the Microstructure and Mechanical Properties of 17-7 PH Stainless Steel Welded by Pulsed Nd-YAG Laser Beam

H. Rafiei *[1], R. Shoja Razavi [2]

[1] Advanced Materials Research Center, Department of Materials Engineering, Najafabad Branch, Islamic Azad University, Najafabad, Iran
[2] Department of Mechanical, Materials and Manufacturing Engineering (MMME), Faculty of Science and Engineering, University of Nottingham Ningbo China (UNNC), Ningbo, China

ARTICLE INFO

Keywords:

Laser Welding, 17-7 PH Stainless Steel, Welding Speed, Pulse Width, Power.

Article history:

Received 30 August 2025
Received in revised form 16 September 2025
Accepted 24 May 2026

ABSTRACT

In this research, the metallurgical investigation of the welding of 17-7 PH steel using the Nd: YAG pulsed laser welding process was conducted. The effect of parameters such as welding speed, laser pulse width and power on welding geometry was evaluated. The microstructure and fracture surface of weld samples were studied using the optical microscope and scanning electron microscope (SEM). Also, in order the tensile, microhardness and impact tests were used to study the mechanical behavior of the joint. It was found that the microstructure of the weld metal of the samples contained skeletal and lathy ferrite as well as austenite. The maximum tensile strength was observed in the sample with power 300, welding speed 2 and pulse width 3.5, and the minimum tensile strength was observed in the sample with power 300, welding speed 2 and pulse width 3. The SEM images of the tensile cross section showed that the failure occurred in all the soft samples. As a result, in this study, the best mechanical and microstructural results were obtained in the welded sample with optimal parameters including power 300, welding speed 2 and pulse width 3.5.

1. Introduction

Semi-Austenite Precipitation Hardening Stainless Steels are used in a variety of applications such as aerospace, marine, nuclear and chemical process due to their favorable combination of excellent mechanical properties and good corrosion resistance [1]. The good corrosion resistance of this steel is attributed to the presence of chromium and the high strength is owing to the presence of homogeneously distributed fine precipitates of intermetallics or elemental phases of alloying elements such as aluminum, titanium, niobium, and copper [2]. 17-7 PH Semi-austenitic stainless-steel sheets are widely used in the military, marine and aerospace industries [3].

Laser welding, as a new technology, has found wide applications in various industries such as automotive, military, aerospace, shipbuilding, electronics, etc. in recent years [4]. Laser beam welding (LBW) has been developed as a process for joining and repairing high-temperature alloys in industry due to its ability to produce welds with high strength, low distortion, low residual stress, stress corrosion cracking and fatigue properties [5-7]. The small weld width, high penetration depth, appropriate

** Corresponding Author*
Email: hr_rafiei@yahoo.com
Address: Advanced Materials Research Center, Department of Materials Engineering, Najafabad Branch, Islamic Azad University, Najafabad, Iran
1. M.S.c, 2. Ph.D

DOI: http://10.22034/IJISSI.2026.2062223.1322
Published by ISSI (Iron & Steel Society of Iran)

strength, and low warping of laser welds, given the need for lightness and resistance to corrosion, aesthetic appearance, elimination of electrode consumption and consequently elimination of machining steps, as well as the possibility of welding inaccessible joints, have led various industries to use this method more [8].

Pulsed Nd-YAG laser welding of 17-7 PH stainless steel is considered one of the most widely used in structural materials in industries such as military, marine, oil and gas industries due to their excellent fatigue and corrosion resistance, thermal and electrical conductivity and acceptable strength [9]. Nowadays, researchers have studied the laser welding of Stainless Steels [10-17]. Recently, Bahrami Balajaddeh and Naffakh-Moosavy [18] studied the Microstructure, mechanical properties, and weldability investigation of the Pulsed Nd: YAG laser welding of 17-4 PH stainless steel. Their results show that the weld metal microstructure was δ-ferrite in a martensite matrix. The presence of δ-ferrite in the weld metal was due to its ferrite PSM and its interdendritic and lath morphologies. Ventrellaa et . al. [19] investigated the Pulsed Nd: YAG laser seam welding of AISI 316L stainless steel thin foils. They reported that the shape and dimensions of the thin foil weld bead depended not only on the pulse energy, but also on the presence of gaps between foils. Bead width, connection width and bead depth increased as the pulse energy increased, and then decreased at the end due to the burnthrough. Baghjari et. al [20] investigated the effect of laser beam position on weld characteristics of AISI 420 stainless steel to Kovar alloy. They reported that the rapid cooling rate during laser welding followed by shifting the laser beam toward SS 420, affects the weight percent of the main chemical elements (Cr, Ni, Fe) and the microstructure in the weld zone. Also, the microhardness results show that the shifting laser beam position from Kovar alloy to SS 420 not only led to the increase of hardness from about 200 to 400HV along the cross-section of the weld zone.

According to the previous studies, the semi-austenitic precipitation hardening stainless steels have good mechanical properties, including good formability and high strength, as well as good corrosion resistance, which has led to their widespread use in the power, petrochemical, nuclear and other industries [21]. The joining of semi-austenitic 17-7 PH stainless steel is widely used in the military, marine and aerospace industries. Many studies have been conducted on the joining of stainless steels, which show that this joining requires a suitable, accessible, easy and cost-effective welding process [22]. Laser welding is one of the most advanced types of fusion welding, which provides the heat required to produce a molten pool and perform the joining process by irradiating a high-energy laser beam to the desired surface [23].

In laser welding, a thin and deep weld is obtained; compared to conventional methods, the energy input to the piece is very low [24]. This property allows laser welding to be used in specific applications where high penetration depth and weld width are required [25]. The laser power can control the diffusion depth and weld width, changing the spatial position of the beam focus relative to the workpiece surface, welding speed, time distribution of energy transfer to the metal (pulsed or continuous), and parameters related to the shielding gas flow, etc [26]. The tiny weld width, high depth, appropriate strength, and low warping of laser welds, due to the need for lightness and corrosion resistance, aesthetic appearance, elimination of electrode consumption and consequently elimination of machining steps, as well as the possibility of welding inaccessible joints, have led various industries to use this method more [27].

Pulsed Nd-YAG fusion welding is one of the available and suitable methods that can be achieved by optimizing the parameters of welding speed, pulse width, and power to achieve appropriate mechanical and microstructural properties. In general, this study aims to investigate the microstructure and mechanical behavior of 17-7 PH steel welds using the Nd: YAG pulsed laser welding process. The same effect of power, welding speed, and width on the joint of 17-7 PH steel has not been observed in previous researchers.

2. Experimental Procedure

In this paper, 17-7 PH stainless steel plates with 1.2mm thickness were used as base metals. The chemical composition and mechanical properties of base metals are presented in Tables 1 and 2., respectively. Elemental analysis of semi-austenitic precipitation of stainless-steel base metal was measured using spark emission spectrometry test by the Foundry Master UV device. Mechanical properties were measured using a 30-ton tensile tester, model INSTRON-4486, made in England, according to ASTM standard-E8.

Table 1. The chemical composition of base metals was used in this paper (Wt. %).

Element	Fe	C	Cr	Mn	Si	Ni	Al
17-7 steel	Base	0.55	17.3	0.76	0.37	7.36	1.05

Table 2. Mechanical properties of the base metals of 17-7 PH steel.

Mechanical characteristics	Tensile strength (MPa)	Yield stress (MPa)	Elongation (%)
17-7 PH steel	1157	953	6

In this research, a 17-7 PH stainless steel plate was selected as a sheet with a specific thickness of 1.2mm and dimensions of 300 × 400mm. The samples were cut using a wire cutter including a cooling system. Fig. 1. shows the schematic of butt-welding joints prepared for welding.

In this study, a pulsed laser welding process (Nd-YAG) was used to produce a suitable joint with a butt joint design. After preparing the semi-austenitic 17-7 PH precipitation hardening stainless steel sheets, the samples were welded using the pulsed laser welding method (Nd-YAG). In order to eliminate the problems related to porosity, the sheets were joined in the presence of an argon shielding gas with a purity of 99.999% with 15 liters per minute flow rate. The welding process (Nd-YAG) was done using a pulsed laser welding machine Nd: YAG model IQL 10 with a maximum power of 400W. The welding parameters are presented in Table 3.

Cross-sectional specimens cut from each joint were prepared by grinding using 60–3000 grits silicon carbide paper and polished with 0.1 µm alumina solution (Al_2O_3), then were attacked with etched solution (10gr $FeCl_3$+ 40ml H_2O+ 6ml HCl +60ml C_2H_5OH) for 10-15 minutes. The IM 420 optical microscope (OM) and SEM in a LE0440i model XL30 were used to examine the microstructure and fracture surface. The mechanical properties were tested with tensile and microhardness tests. According to ASTM: E8, three cross-sectional specimens were prepared [28]. The tensile test was performed using the INSTRON-4486 machine. The Vickers micro-hardness was carried out according to the ASTM E-92 standard [29]. The microhardness test was performed a load of 100g for 10s duration by using a Shimadzu micro indention device. Also, a Charpy impact test was performed according to ASTM E23 standard using a Centam model SIT-300 impact test machine at ambient temperature [30].

3. Results and Discussion

3.1. Macrostructure

3.1.1. Effect of Welding Speed and Laser Power on the Constant Pulse Width

Fig. 2. shows the Weld Macrostructure (weld depth and width) with different power and welding speed in a constant pulse width of 3.5. Also, Fig. 3. shows the ratio of input heat ($\frac{P}{V}$) to the depth and width of the weld sample welded with 250W power with different speeds. The macrostructure of the samples shows that the trend of increasing weld pool depth with increasing power has a steeper slope than the trend of increasing weld pool width, so by increasing power from 200 to 250W, the weld pool depth was increased significantly. This can indicate the transition from conductive mode to keyhole mode. In the conductive mode, the laser beam is largely reflected so its energy is wasted. Increasing the beam power increases the surface evaporation of the metal and the beam penetrates the material. In this case, the reflected beam collision to the inner surface and some of it is absorbed, reducing energy loss and increasing the process efficiency, causing a sudden increase in the depth of the pool. Fig. 3. clearly illustrates the increase in weld

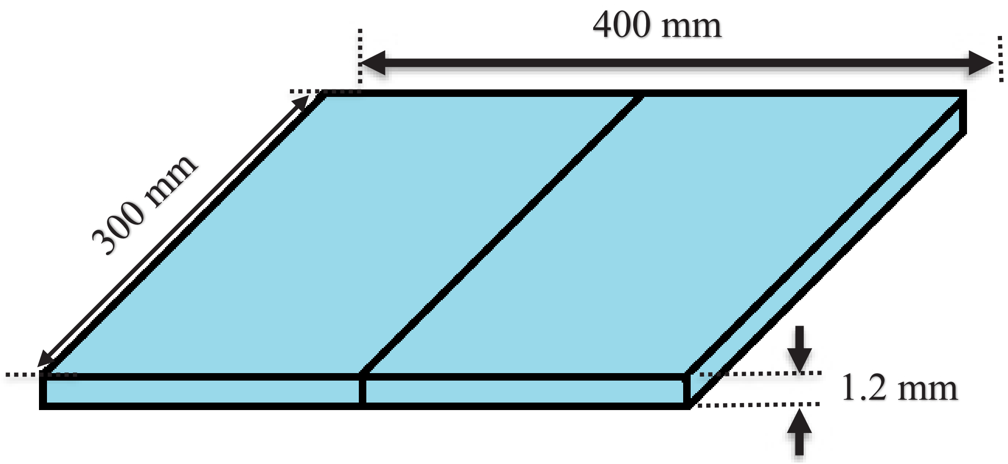

Fig. 1. Schematic of Butt-welding joints (mm).

Table 3. The laser welding parameters.

Sample No.	Power (W)	Frequence (Hz)	Welding speed (mm/s)	Pulse width (ms)	Heat input (kJ/mm)
250-V2-3	250	20	2	3	0.75
300-V2-3.5	300	20	2	3.5	1.05
300-V3-3.5	300	20	3	3.5	0.70

pool width for samples welded at a constant speed of 4mm/s and constant power. However, for samples welded at lower speeds, the effect of increased pulse width is less significant. This can be attributed to the higher heat input at lower welding speeds, which is dominant over the effect of pulse width.

It should be noted that the shape and geometry of the weld pool are also affected by the percentage of overlap. By observing the weld pool surface in samples with low welding speed and samples with high welding speed, it is inferred that in conditions where the percentage of overlap is low, the shape and geometry of the upper section of the molten pool, which is in fact the point of impact of the pulses on the part, is in the form of a circle that can be distinguished due to the degree of their overlap on each other. In other words, in this case, the melting boundary lines can be identified. These identifiable lines are in fact the solidification boundaries between two consecutive pulses that arise due to the pulsed nature of the power source. As a result, a high cooling rate is created at high welding speeds or low frequencies. In such conditions, with a high cooling rate, the previous pulse can be completely frozen before it hits it.

As the overlap increases, it changes from a circular shape to an oval shape, and then at lower speeds it becomes a straight line, in which case the pulse weld becomes a continuous weld.

Welding depth and width with constant pulse width are shown in the Tables 4 and 5. respectively. According to Fig. 4. and Table 4. it can be seen that at a constant welding speed and pulse width, the weld depth and width increase with increasing welding power. Fabian [8]

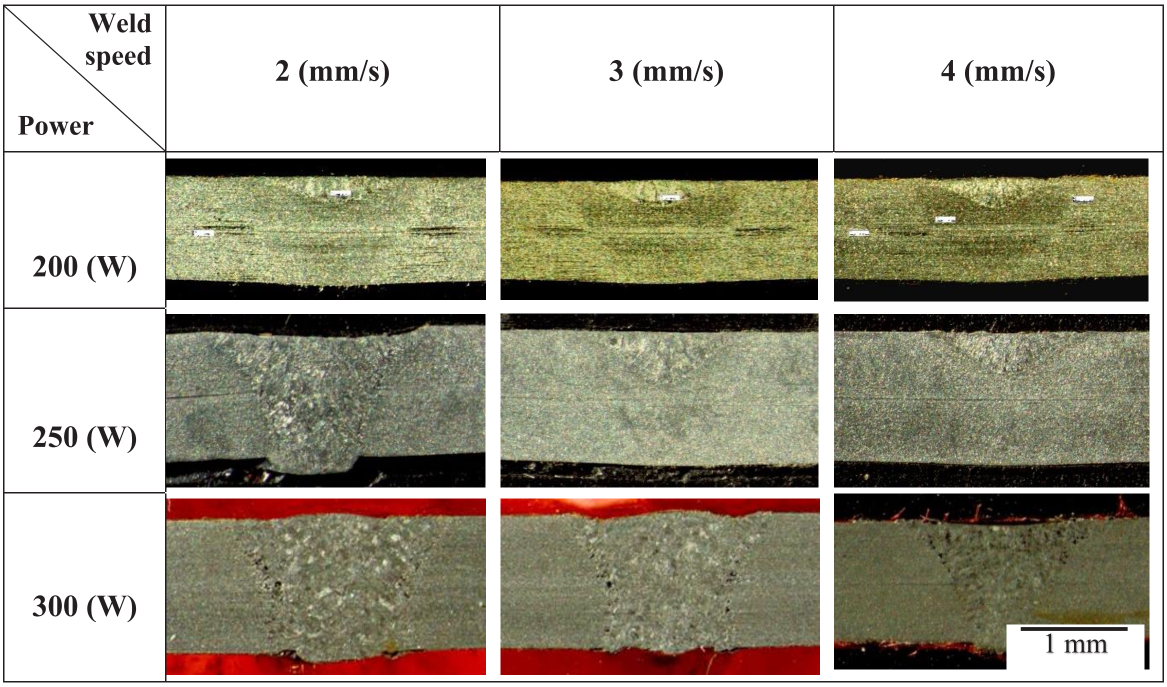

Fig. 2. Depth and width of Weld With constant pulse width 3.5.

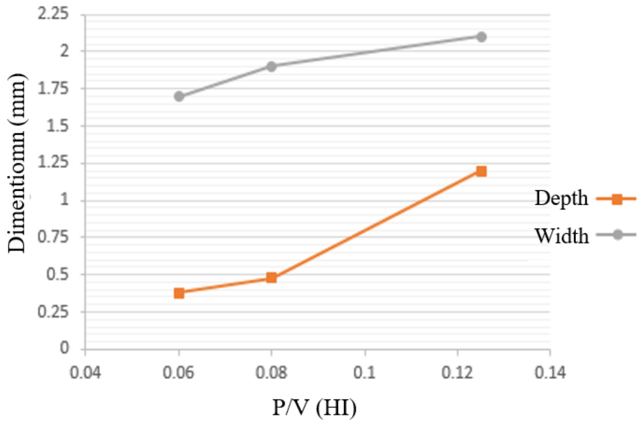

Fig. 3. Graph of heat input ratio $(\frac{\rho}{V})$ against weld depth and width of a sample welded with a 250W power at different weld speeds.

studied that the ratio of power to welding speed $(\frac{\rho}{v})$ is directly related to the input heat. The transition of the weld pool from conduction to keyhole mode can be observed visually based on the weld cross-section. As shown in the transverse cross-sections of the samples, the welds produced at a laser power of 200W remain in conduction mode across all three welding speeds. However, for the welds produced at 250W, keyhole mode is initially observed at a welding speed of 2mm/s. As the welding speed decreases, the weld pool transitions back to conduction mode. Han et al. [7] investigated the effect of welding speed and reported that decreasing the speed increases the percentage of pulse overlap. Since a higher overlap result in a greater number of pulses per unit length and consequently an increase in energy input per unit length, reducing the welding speed leads to greater weld depth and width. This phenomenon is clearly illustrated in Tables 4 and 5. In this case, a fraction of each pulse area is affected by the heat generated from the overlapping subsequent pulses, leading to an overall increase in heat input. Furthermore, the increase in pulse overlap has a more significant effect on weld depth than on weld width.

3.1.2. Effect of Welding Speed and Pulse Width at Constant Power

Fig. 4. presents the macrostructure of the welds produced at a constant laser power of 300W while varying the pulse width and welding speed. As observed, an increase in welding speed effectively reduces the number of pores within the welds. At a welding speed of 3mm/s, porosity is nearly eliminated. Additionally, pore formation is more sensitive to welding speed than to arc current. At lower welding speeds, porosity becomes more pronounced, particularly under high arc current conditions. As shown in Fig. 4., the porosity observed in the upper region of the weld bead disappears under higher arc current. In this scenario, the molten pool undergoes increased pressure and expands accordingly [31]. Consequently, gas bubbles in the upper region of the weld pool escape more easily, leading to a reduction in porosity in the upper section of the weld bead.

Table 4. Welding depth with constant pulse width.

Speed / Power	2(mm/s)	3(mm/s)	4(mm/s)
200 W	0.23	0.21	0.2
250 W	1.2	0.48	0.38
300 W	1.2	1.2	1.2

Table 5. Weld width with constant pulse width.

Speed / Power	2(mm/s)	3(mm/s)	4(mm/s)
200 W	0.9	0.7	0.7
250 W	2.1	1.9	1.7
300 W	2.25	2.2	2

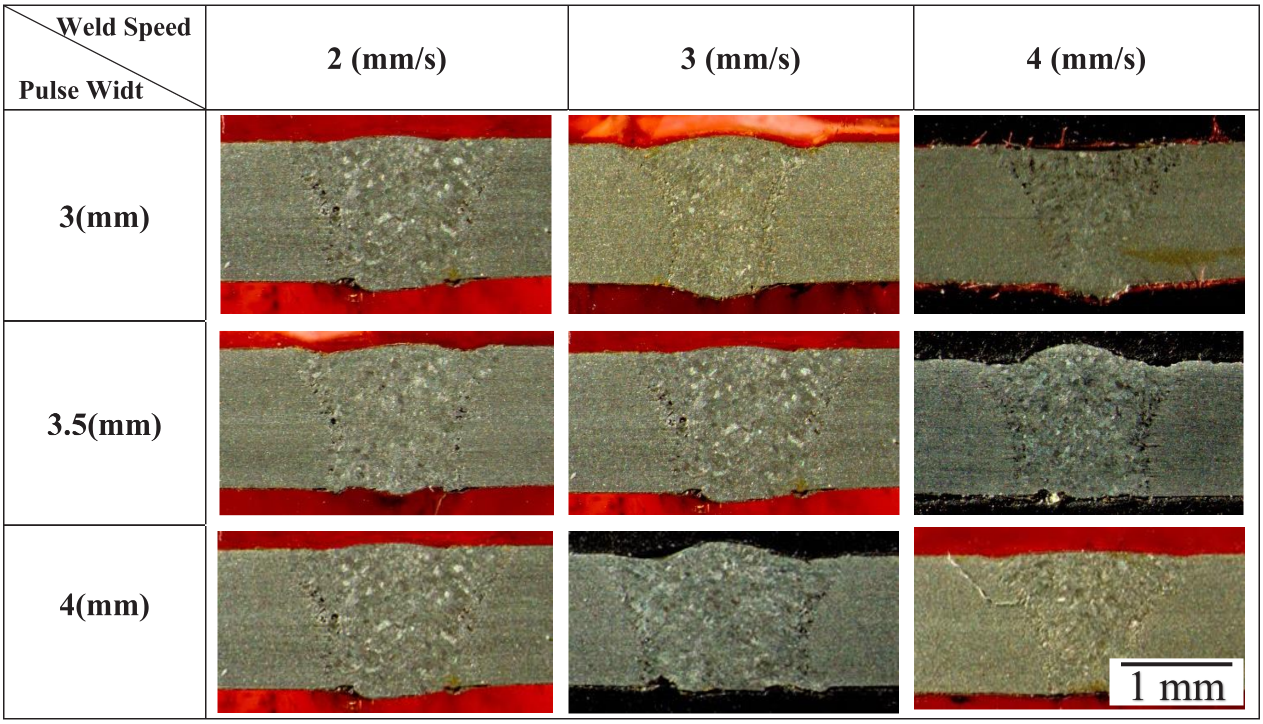

Fig. 4. Weld depth and width with constant power of 300W.

In this series of experiments, the effect of increasing pulse energy, accompanied by an increase in pulse width and consequently heat input, was investigated while maintaining constant power. As the heat input changes, the dimensions of the weld pool change at a higher rate. Fig. 5. shows the macrostructure of the welds (weld depth and width) for varying power and pulse width at a constant welding speed of 2mm/s. As observed in Fig. 5., in this study changing the pulse width does not significantly affect the weld depth or width when compared to the effects of power and welding speed.

In laser welding, the pulse overlap effect refers to the spatial and temporal overlap of laser pulses in the welding process, which has a direct effect on the quality, depth, and strength of the weld. This phenomenon is especially important in welding with pulsed lasers (such as Nd:YAG or fiber lasers), where laser pulses with a specific frequency and energy are used to melt and join materials. important factors in overlap welding are spot size, speed scanning, pulse repetition Rate, pulse duration, pulse energy and pulse energy. Table 6. shows the percentage of pulse overlap. Fig. 6. shows the weld surface (overlap) in 250-v2-3, 300-v2-3.5, and 300-v3-3.5 samples. By observing the weld pool surface in samples with low welding speed and samples with high welding speed, it is inferred that in conditions where the percentage of overlap is low, the shape and geometry of the upper section of the molten pool, which is in fact the point of impact of the pulses on the part, is in the form of a circle that can be distinguished due to the degree of their overlap on each other. In other words, in this case, the melting boundary lines can be identified. These identifiable lines are in fact the solidification boundaries between two consecutive pulses that are created due to the pulsed nature of the power source, which is a result of the high cooling rate at high welding speeds or low frequencies. In such conditions, with a high cooling rate, the previous pulse can be completely frozen before it hits it. The shape of the upper surface of the weld pool changes from circular to elliptical with increasing overlap, and then to a straight line at lower speeds, in which case pulse welding becomes continuous welding. The figure below shows an example of the overlap effect with increasing pulse speed. According to the following relationship, the overlap percentage is calculated.

Eq.(1)

$$\text{Overlap} = \left(1 - \frac{\text{welding speed}}{\text{pulse frequency} \times \text{spot diameter}}\right) \times 100$$

3.2. Microstructure

3.2.1. Microstructure of Base Metal

Fig. 7. shows the microstructure of the 17-7 PH semi-austenitic hardened steel base metal. 17-7 PH semi-austenitic steel (UNS S17700) contains 17wt.% chromium, 7wt.% nickel and 1.2wt.% aluminum. According to Fig. 2., the microstructure of 17-7 PH semi-austenitic hardened steel contains austenite grains as matrix and some skeletal delta ferrite (δ). Also, as shown in the 17-7 PH semi-austenitic hardened steel microstructure delta ferrite strands are elongated in the rolling direction. Microstructural investigation of the base metal is consistent with previous studies [3].

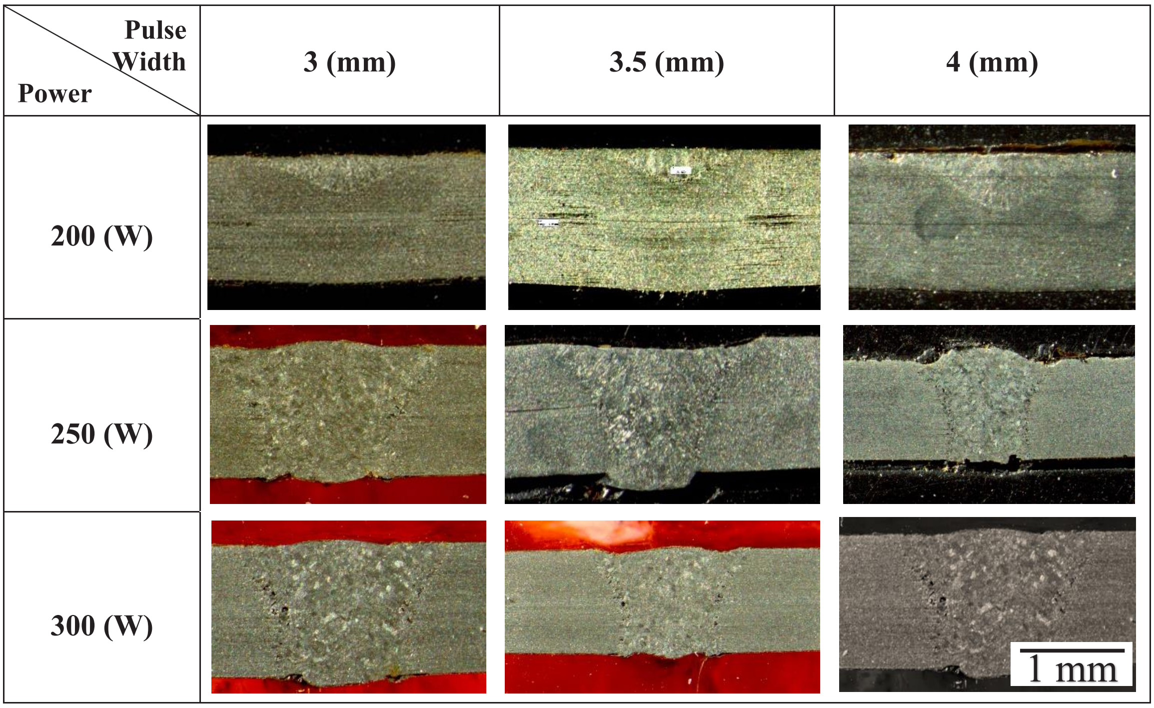

Fig. 5. Weld depth and width with a constant welding speed of 2mm/s.

Table 6. percentage of pulse overlap (%).

Sample No.	Welding speed (mm/s)	overlap (%)
250-V2-3	2	83
300-V2-3.5	2	83
300-V3-3.5	2	75

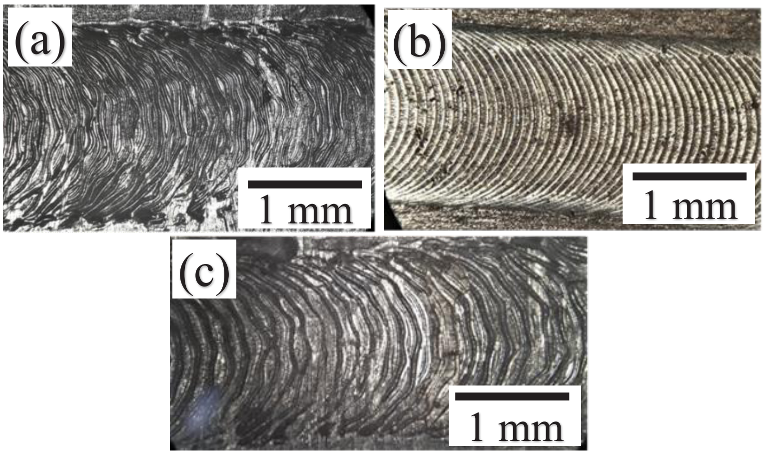

Fig. 6. View of the weld surface (overlap) in samples (a) 250-v2-3, (b) 300-v2-3.5, and (c) 300-v3-3.5.

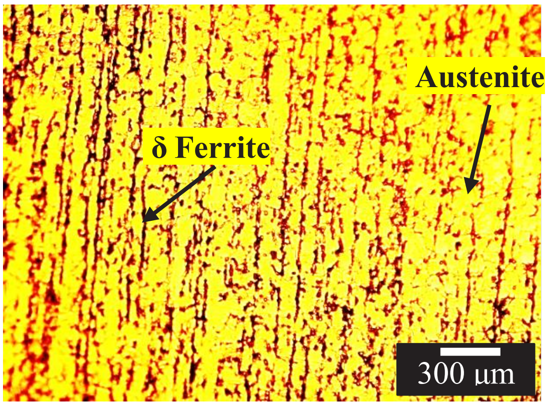

Fig. 7. Microstructure of 17-7 PH stainless steel base metal.

3.2.2. Microstructure of Base Metal-Weld Metal Interface Region (HAZ)

Fig. 8. presents the microstructure of the base metal-weld metal interface region of samples 250-v2-3, 300-v2-3.5, and 300-v3-3.5 specimen. As shown in Fig. 8., the delta ferrite increased in the HAZ zone from the base metal into the weld metal. In this region, the morphology of delta ferrite was observed coaxially. Also, due to the low heat transfer coefficient in semi-austenitic stainless steels the width of the heat-affected zone is very narrow. The heat input of samples 250-v2-3, 300-v2-3.5 and 300-v3-3.5 is 0.75, 1.05 and 12.25, respectively.

By increasing the input heat, the amount of delta ferrite in the interface was increased. This seems logical, because the amount of delta ferrite formation is low due to the slow transformation of austenite to ferrite and the rapid thermal cycle of the heat affected zone. With increasing input heat, the amount of heat applied to the HAZ zone increases so the amount of ferrite increases. Also, according to Fig. 8., larger ferrite regions located at the boundaries of martensitic and austenitic grains, such as inside the plate-shaped austenitic boundaries, are observed in the overheated area in the heat- affected zone. Also, the results showed that the microstructure of this region is the same in all samples and no change in their microstructure occurred.

3.2.3. Microstructure of Weld Metal

Fig. 9. shows the microstructure of the weld metal region of 250-v2-3, 300-v2-3.5 and 300-v3-3.5 specimen. As shown the Fig. 9., the skeletal and lathy ferrite in the austenite matrix were formed in the weld metal. This morphology of ferrite phase forms when the cooling rate is medium, or the Cr_{eq}/Ni_{eq} ratio is in the ferrite-austenite (FA) area. This was because of developing ferrite-consuming austenite and continued until sufficient enrichment of ferrite former elements (Cr and Mo), depletion of austenite former elements and stabilizing at lower temperatures where diffusion is limited [29]. Previous studies have shown that porosity was not a major issue in joining 17-4 PH steels by arc welding processes (GTAW and SMAW), and argon was typically chosen as the shielding gas. However, severe porosity was observed in weld beads produced by arc welding and laser arc welding. Different methods for stabilizing keyholes and preventing porosity have been investigated by a number of researchers [31].

Kawahito et al. [31] found that high welding speed can cause keyhole perforation and eliminate porosity during laser welding of AISI 304 stainless steel. Katayama et al. [10] studied the effect of a plasma plume on the weld penetration are greatly different between CO_2 laser welding and YAG, disk or fiber laser welding. They reported that the spattering leading to the formation of underfilled weld beads is controlled by inclining the laser beam. Porosity is formed from bubbles generated from the tip of the keyhole at low welding speed or from the middle part of the keyhole at high laser power density. Cracking easily occurs in pulsed spot welding of aluminum alloys.

Fig. 10. presents the microstructure of the weld metal for sample 300-v2-3.5 at high magnification. As shown in Fig. 10., the microstructure of the sample is characterized by a ferrite-austenite structure. The delta ferrite is observed to form in a skeletal and columnar arrangement within the austenitic matrix. The presence of ferrite with a dendritic and network morphology can be attributed to the Cr_{eq}/Ni_{eq} ratio and the high cooling rate during pulsed laser welding. Furthermore, as shown in Fig. 9., the microstructure of the weld metal exhibits columnar grains. This is due to a reduction in the thermal gradient (G) in certain areas, especially when the base metal thickness is low. This decrease in the thermal gradient leads to an increase in the growth rate (R), resulting in a reduction of the G/R ratio. As the G/R ratio decreases, the solidification mode transitions from planar to cellular and eventually to dendritic [32]. Moulian et al. [34] reported that the microstructure of the samples exhibited a fine-grained, predominantly cellular-dendritic structure in the molten zone. This type of microstructure is a result of rapid cooling, which is typical in laser welding processes. During solidification, the formation of a specific solid structure is determined by the G/R ratio (where G is the temperature gradient and R is the growth rate). When the G/R ratio is high, cellular structures tend to form, as opposed to dendritic structures.

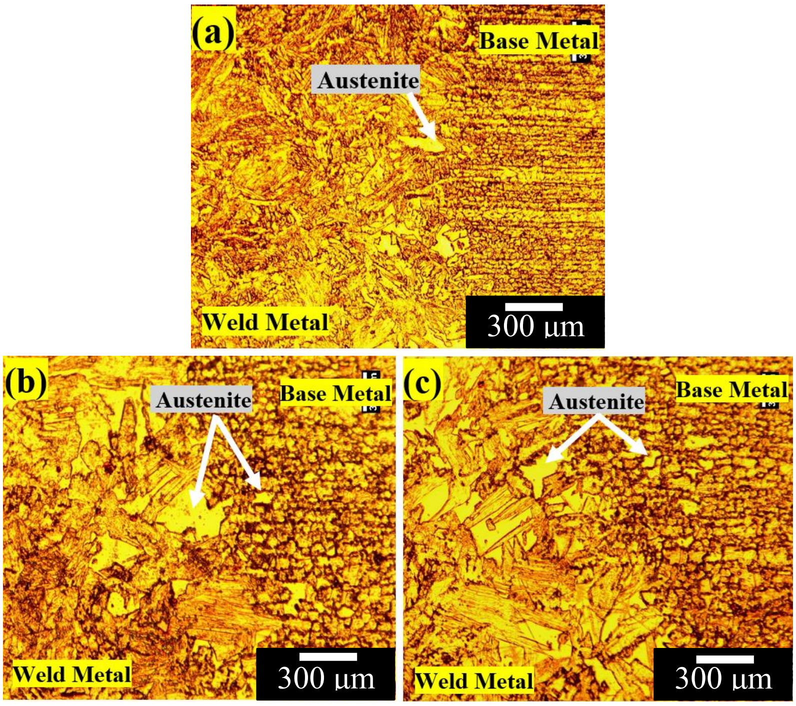

Fig. 8. Microstructure of the interface of the base metal and the weld metal of (a) 250-v2-3, (b) 300-v2-3.5 and (c) 300-v3-3.5 samples.

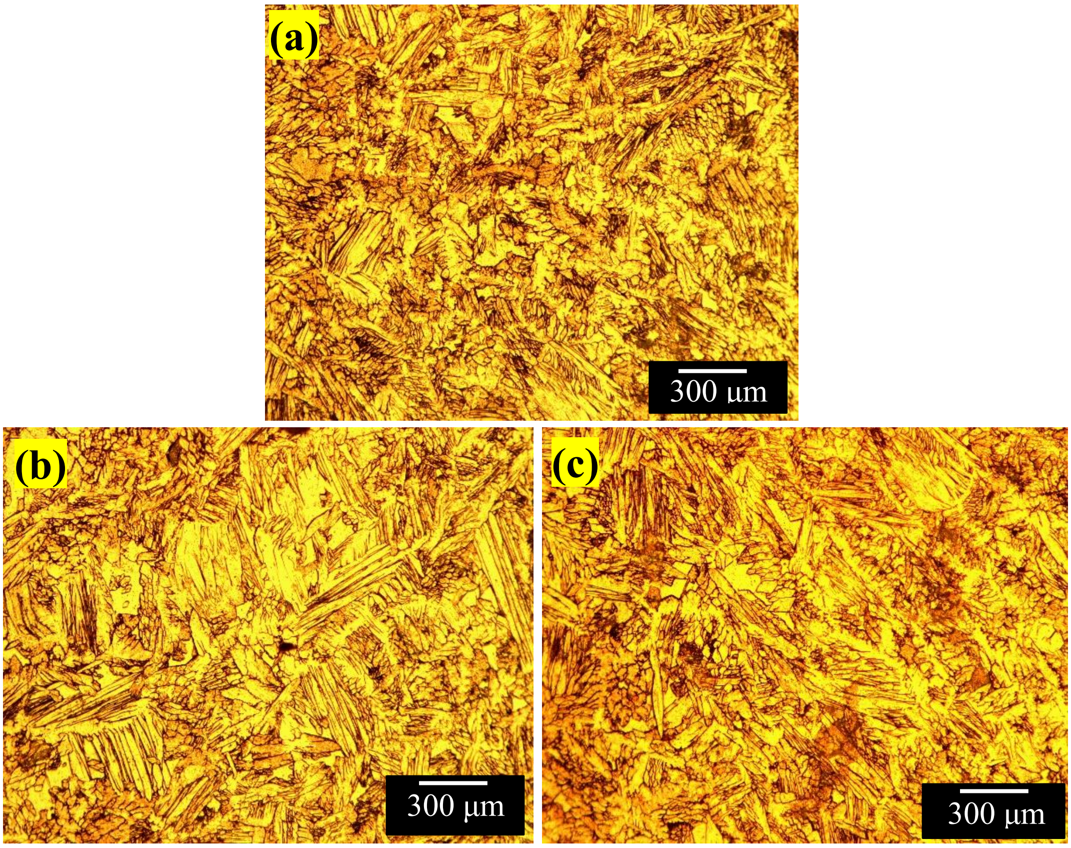

Fig. 9. Microstructure of the weld metal region of (a) 250-v2-3, (b) 300-v2-3.5 and (c) 300-v3-3.5 speciment.

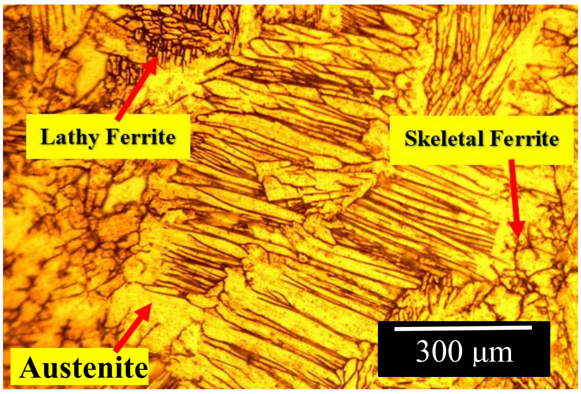

Fig. 10. Microstructure of the weld metal area of sample 300-v2-3.5.

3.3. Tensile Test

Fig. 11. shows the Stress-strain diagram of samples 250-v2-3, 300-v2-3.5 and 300-v3-3.5. The effects of welding parameters on the tensile strength of 17-7 PH stainless steel welded by pulsed Nd-YAG laser beam are shown in Table 7. As it can be seen in Table 7., the tensile strength of the 250-v2-3, 300-v2-3.5, and 300-v3-3.5 speciment was about 414, 989, and 702 MPa, respectively. According to Table 6., it is observed that the highest tensile strength of the weld was obtained in the sample welded with a beam power of 300, a welding speed of 2, and a pulse width of 3.5. Also, according to Fig. 11., it can be seen that the elongation of the 250-v2-3, 300-v2-3.5 and 300-v3-3.5 samples is about 5%, 35.5% and 20% respectively, so the maximun elongation was observed in the sample welded with a beam power of 300, welding speed of 2 and pulse width of 3.5. Fig. 12. shows the failure location of the the samples. According to Fig.12., the failure in the 250-v2-3, 300-v2-3.5 and 300-v3-3.5 occurred in the weld metal, base metal and HAZ Zone, respectively.

Quan et al. [32] reported that when the pulse power is too low, the weld pool does not have enough time to form and incomplete welding occurs. With an excessive increase in the pulse power, the grains in the weld metal and in the HAZ become coarser. The width of the heat-affected zone also increases and the discontinuity becomes more severe. Some precipitates can exist intergranularly and even continuously along the grain boundary. These microstructural changes cause the formation of weld joints and reduce tensile properties. According to Table 7., it is observed that the Ultimate tensile strength increased with increasing power. In samples 300-v2-3.5 and 300-v3-3.5, the Ultimate tensile strength decreased while keeping the power constant and increasing the welding speed. The results showed that the highest Ultimate tensile strength was obtained in the sample welded with a power of 300 and a welding speed of 2.

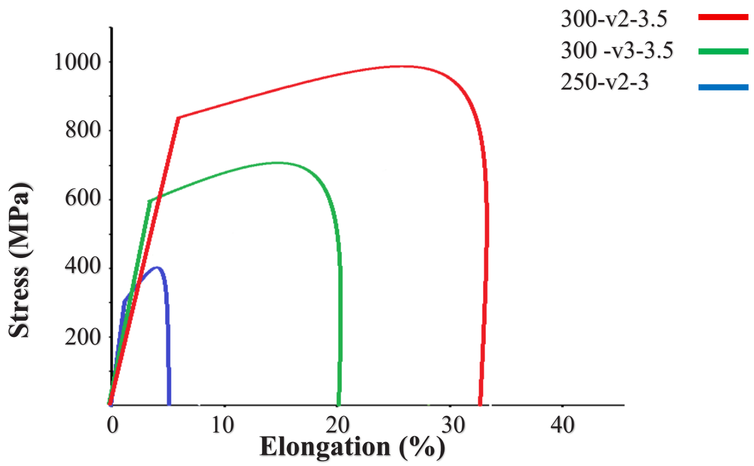

Fig. 11. Stress-strain diagram of samples (a) 250-v2-3, (b) 300-v2-3.5 and (c) 300-v3-3.5.

Table 7. Tensile strength and elongation of welded samples.

sample	Ultimate tensile strength (MPa)	Elongation (%)
250-v2-3	414	5
300-v2-3.5	989	33.5
300-v3-3.5	702	20

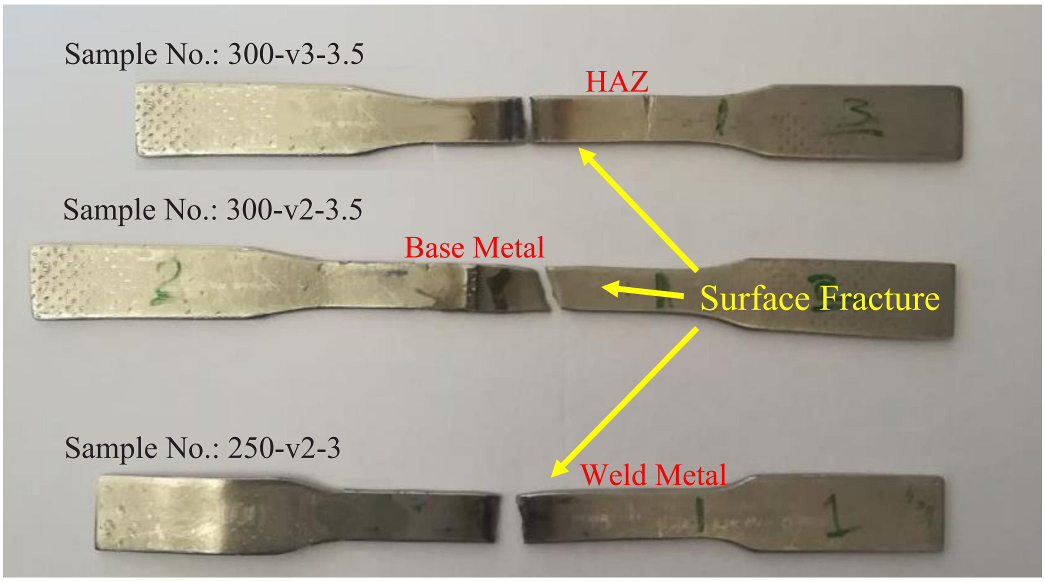

Fig. 12. Tensile test samples after testing.

3.4. Fracture Surface

SEM fracture images of 250-v2-3, 300-v2-3.5, and 300-v3-3.5 specimens are presented in Fig. 13. According to Fig. 13., it is observed that the fracture surfaces of all specimens contain small dimples and funnel-shaped holes, which indicates that the fracture indicating brittle fracture mode. The only difference is the size of the dimples and holes. Thus, the smaller the holes, the more brittle the fracture occurred, and the larger the holes, the more ductile the fracture occurred. As can be seen in the images, the number of holes in the image of sample 250-v2-3 is less and, as expected, the fracture of this sample is more brittle than the other samples. Also, considering that this sample has fractured in the weld area.

The only difference observed between the samples lies in the size of the dimples and voids. Specifically, smaller voids correspond to a more brittle fracture behavior, while larger voids result in a more ductile fracture. As shown in the images, the sample 250-v2-3 has fewer voids, and as expected, the fracture of this sample is more ductile compared to the others. Additionally, it is worth noting that this sample failed in the weld zone.

3.5. Microhardness Test

Fig. 14. illustrates the horizontal microhardness profile of the 250-v2-3, 300-v2-3.5 and 300-v3-3.5 welded specimens. As shown in Fig. 14., the microhardness of the base metal of the17-7 PH semi-austenitic precipitated stainless steel was found to be about 224HV. Ferrite is a harder phase compare to the austenite phase, which increases the hardness. According to Fig. 14., it can be seen that the microhardness of the weld zone for samples 250-v2-3, 300-v3-3.5 and 300-v2-3.5 was about 227 Vickers, 219 Vickers and 240 Vickers, respectively. According to Fig. 11., it can be seen that the microhardness of the weld zone for 250-v2-3, 300-v3-3.5 and 300-v2-3.5 speciments are 227, 219 and 240 Vickers, respectively.

Since hardness is directly related to the phases formed in the microstructure and the volume fraction of these phases, changes in hardness can be attributed to alterations in the phase percentage and the cooling rate of the material during and after solidification. As observed, hardness decreases from the center of the weld towards the edges. This phenomenon can be explained by the lower cooling rate and the maximum thermal cycle temperature from the center to the edges, leading to different phase transformations in various regions of the weld pool and consequently, differing microhardness values. Generally, hardness is higher in the center of the weld pool compared to the edges of the weld pool and the base metal. The higher hardness in the center is due to the higher percentage of ferrite in this area. In contrast, the reduced hardness near the weld pool boundary is attributed to the higher percentage of austenite in that region. This trend indicates that the higher the hardness, the greater the proportion of the ferrite phase. Microhardness testing was conducted on several cross-sections of weld samples with different overlap factors. The results of the hardness study are shown in Fig. 14. Mirakhouri and Ghaini [33]

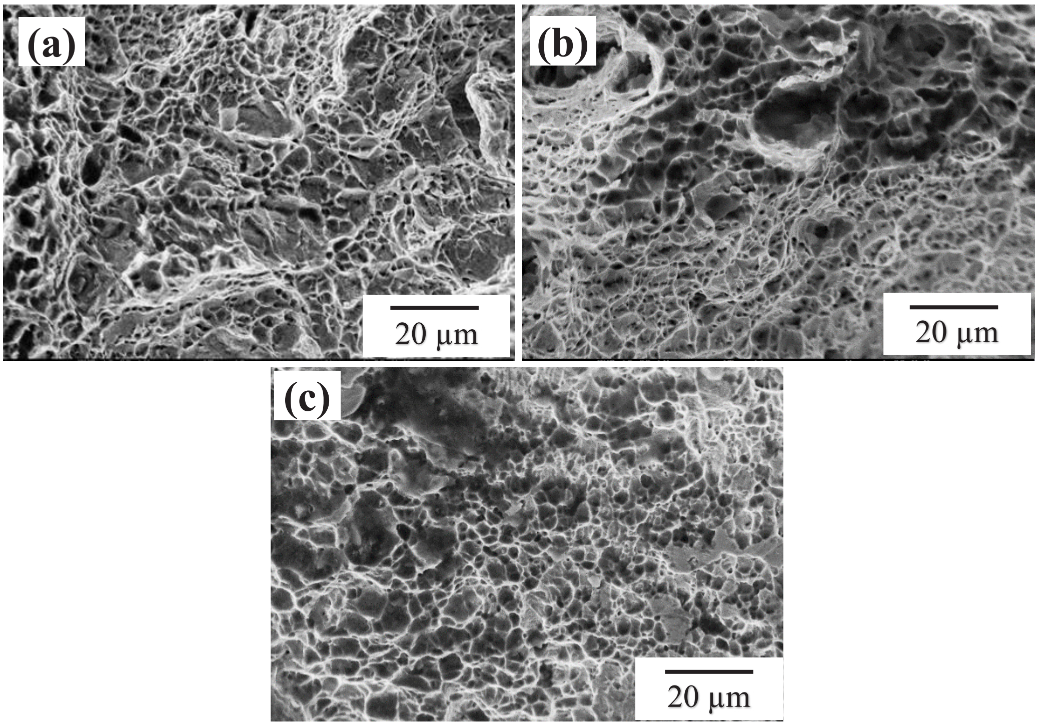

Fig. 13. Failure surface of samples for: (a) 250-v2-3, (b) 300-v2-3.5, and (c) 300-v3-3.5.

demonstrated that the higher hardness observed in the weld center could be due to a greater volume of ferrite phase in this region. The results indicate that the highest microhardness value corresponds to sample 300-v2-3.5, while the lowest microhardness is observed in sample 300-v3-3.5. The slight increase in hardness is associated with a higher volume of skeletal ferrite phase in 17-7 PH during cooling. The microhardness test results also show that the microhardness in sample 300-v2-3.5 is higher compared to the other two samples, which aligns with the tensile test results.

3.6. Impact Test Results

Fig. 12. shows the average of the Charpy V-notch impact test and the average absorbed energy results of different weld metals. As shown in Fig. 12., the impact energy of 250-v2-3, 300-v2-3.5, and 300-v3-3.5 speciments is 37, 65, and 48 joules, respectively. The results show that the maximum impact energy is related to the 300-v2-3.5 sample and the minimum impact energy is related to the 250-v2-3 sample. The results obtained in this section align with the findings from the tensile tests and the microstructural evaluations.

4. Conclusions

In this paper, the metallurgical investigation of 17-7 PH steel welding using Nd-YAG laser method was carried out, and the effect of parameters such as welding speed, laser pulse width, and power on weld geometry and mechanical properties including microhardness and tensile strength and the microstructure was also considered. The following results were obtained:

- The microstructural investigations showed an increase in delta ferrite in the heat-affected zone (HAZ) between the weld metal and base metal. The microstructure of the weld metal consisted of skeletal ferrite, columnar ferrite, and, in some areas, networked ferrite alongside austenite. The skeletal or creamy-shaped ferrite morphology forms when the cooling rate is moderate or when the Cr_{eq}/Ni_{eq} ratio is in the ferrite-austenite (FA) range.
- The tensile strength of the 250-v2-3, 300-v2-3.5 and

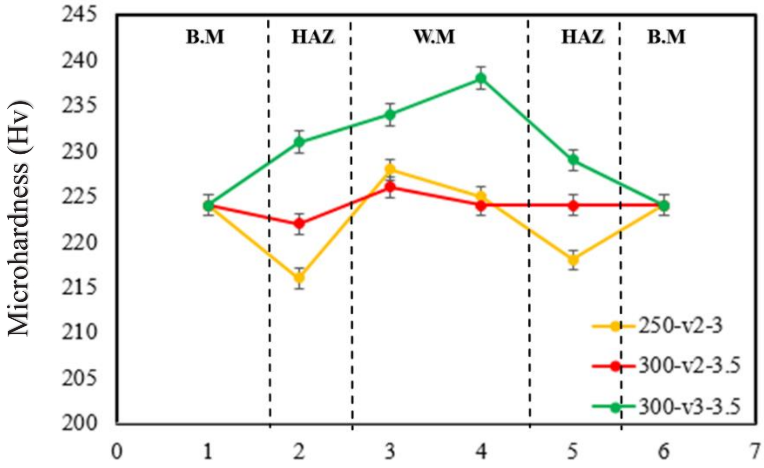

Fig. 14. Microhardness test results of the speciment.

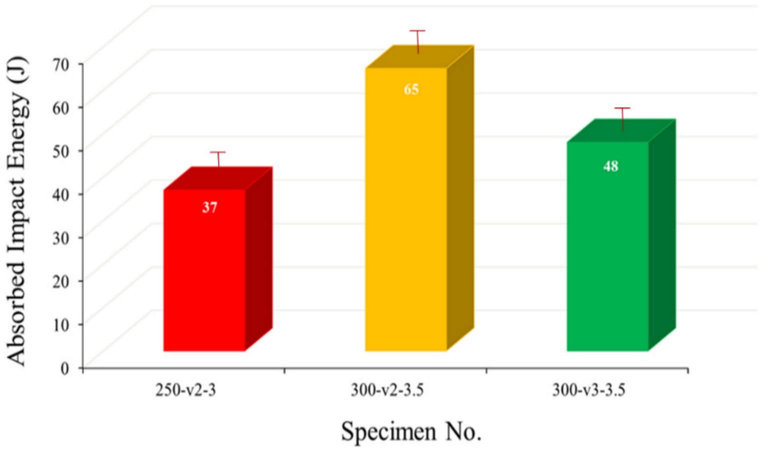

Fig. 15. The average of Charpy V-notch impact energy for different weld metals at 27°C.

350-v2-3.5 samples was found to be about 414MPa, 989MPa and 702MPa respectively. The highest tensile strength was achieved in sample 300-v2-3.5.
- The SEM results of the fracture surfaces indicated the presence of small dimples and funnel-shaped pores, with ductile fracture occurring in all samples. The only difference was the size of the dimples and pores.
- The microhardness test showed minimal variation, which can be attributed to the uniform microstructure of the weld metals. However, the best hardness results were observed in the 300-v2-3.5 sample.
- The impact energy values for the samples were 37 J for 250-v2-3, 65 J for 300-v2-3.5, and 48 J for 300-v3-3.5. The maximum impact energy was found in sample 300-v2-3.5, while the minimum was in sample 250-v2-3.
- In this study, the weld sample with a laser power of 300W, welding speed of 2mm/s, and pulse width of 3.5ms exhibited the best mechanical properties. It and was confirmed to be free of weld defects with an acceptable appearance.

Reference

[1] Michael F, Stainless steels for design engineers, Materials Park (OH): ASM International. 2008.
[2] McGuire M.F, Stainless steels for design engineers, Materials Park (OH): ASM International. 2008.
[3] Burnett H.C, Duff R.H, Vacher H.C, Identification of metallurgical reactions and their effect on the mechanical properties of 17-7 PH stainless steel, J Res Natl Bur Stand C Eng Instrum. 1962; 66C: 113-9.
[4] Peng Y, Tian Z.L, Chen W.Z, et al. Laser welding of ultra-fine-grained steel SS400, Iron Steel Res Int. 2003; 10: 32-36.
[5] Malek Ghaini F, Hamedi M.J, Torkamany M.J, Sabbaghzadeh J, Weld metal microstructural characteristics in pulsed Nd: YAG laser welding, Scr Mater. 2007; 56: 955-958.
[6] Dawes C, Laser welding: a practical guide, Abington: Abington Publishing. 1992.
[7] Han W.J, Byeon J.G, Park K.S, Welding characteristics of Inconel plate using a pulsed Nd: YAG laser beam, J Mater Process Technol. 2001; 113: 234-237.
[8] Bagger C, Olsen F.O, Review of laser hybrid welding, J Laser Appl. 2005; 17.
[9] Torabi A, Kolahan F, Optimizing pulsed Nd: YAG laser beam welding process parameters to attain maximum ultimate tensile strength for thin AISI 316L sheet using response surface methodology and simulated annealing algorithm, Opt Laser Technol. 2018; 103: 300-310.
[10] Katayama S, Kawahito Y, Mizutani M, Elucidation of laser welding phenomena and factors affecting weld penetration and welding defects, Phys Procedia. 2010; 5:9-17.
[11] Fernandes F.A.O, Oliveira D.F, Pereira A.B, Optimal parameters for laser welding of advanced high-strength steels used in the automotive industry. Procedia Manuf. 2017; 13: 219-226.
[12] Akbari Mousavi S.A.A, Sufizadeh A.R, Metallurgical investigations of pulsed Nd: YAG laser welding of AISI 321 and AISI 630 stainless steels, Mater Des. 2009; 30: 3150-3157.
[13] Baghjari S.H, Akbari Mousavi S.A.A, Effects of pulsed Nd: YAG laser welding parameters and subsequent post-weld heat treatment on microstructure and hardness of AISI 420 stainless steel, Mater Des. 2013; 43: 1-9.
[14] Zhang P, Jia X, Yu Z, Shi H, Li S, Wu D, Yan H, Ye X, Chen J, Wang F, Tian Y, A review on the effect of laser pulse shaping on the microstructure and hot cracking behavior in the welding of alloys, Opt Laser Technol. 2021; 140: 107094.
[15] Jia X, Luo J, Li K, Wang C, Li Z, Wang M, Jiang Z, Veiko V.P, Duan J, Ultrafast laser welding of transparent materials: from principles to applications, Int J Extrem Manuf. 2025; 7: 1-46.
[16] Elsheikh A, Omer M.A.E, Basem A, Faqeha H, Alsaati A.A, Thangaraj M, Essa F.A, Shanmugan S, Ramesh B, Sathyamurthy R, Ma N, Recent advances and future prospects of laser welding technology for polymeric materials: a review, J Mater Res Technol. 2024; 35: 7417-7440.
[17] Wang Z, Gao M, Numerical simulations of oscillating laser welding: a review, J Manuf Process. 2024; 119: 744-757.
[18] Bahrami M, Balajaddeh A, Naffakh-Moosavy H, Pulsed Nd: YAG laser welding of 17-4 PH stainless steel: microstructure, mechanical properties, and weldability investigation. Opt Laser Technol. 2019; 119:105651.
[19] Ventrella V.A, Berretta J.R, Rossi W.D, Pulsed Nd: YAG laser seam welding of AISI 316L stainless steel thin foils, J Mater Process Technol. 2010; 210: 1838-1843.
[20] Baghjari S.H, Gholambargani M, Akbari Mousavi S.A.A, Application of pulsed Nd: YAG laser welding to investigate the effect of laser beam position on weld characteristics of AISI 420 stainless steel to Kovar alloy, Lasers Manuf Mater Process. 2019; 6(4).
[21] Deepak J.R, Anirudh R.P, Saran Sundar S, Applications of lasers in industries and laser welding: a review, 2023.
[22] Kurc-Lisiecka A, Lisiecki A, Laser welding of stainless steel, Achiev Mater Manuf Eng. 2020; 98: 32-40.
[23] Landowski M, Influence of parameters of laser beam welding on the structure of 2205 duplex stainless steel, Biul Inst Spawalnictwa. 2019; 63(5): 21-31.
[24] Lisiecki A, Kurc-Lisiecka A, Automated laser welding of AISI 304 stainless steel by disk laser, Arch Metall Mater. 2018; 63: 1663-1672.
[25] Quintino L, Costa A, Miranda R, Yapp D, Kumar V, Kong C.J, Welding with high-power fiber lasers: a

preliminary study, Mater Des. 2007; 28: 1231-1237.
[26] Kou S, Welding metallurgy, 2nd ed. Hoboken (NJ): John Wiley & Sons. 2003.
[27] Duley W.W, Laser processing and analysis of materials, New York (NY): Plenum Press. 1983.
[28] ASTM International. ASTM E8/E8M-00. Standard test methods for tension testing of metallic materials. West Conshohocken (PA): ASTM International; 2000.
[29] ASTM International. ASTM E92. Standard test methods for Vickers hardness and Knoop hardness of metallic materials. West Conshohocken (PA): ASTM International.
[30] ASTM International. ASTM E23. Standard test methods for notched bar impact testing of metallic materials. West Conshohocken (PA): ASTM International.
[31] Liu W, Ma J, Atabaki M.M, Pillai R, Kumar B, Vasudevan U, Sreshta H, Kovacevic R, Hybrid laser-arc welding of 17-4 PH martensitic stainless steel, Lasers Manuf Mater Process. 2015; 2: 74-90.
[32] Sadeghi B, Sharifi H, Rafiei M, Abbasian A.R, Saebnoor E, Microstructural, mechanical and corrosion properties of dissimilar joint between AISI 321 stainless steel and ASTM A537 CL1 structural steel produced by GTAW process, Metall Res Technol. 2019; 116: 110.
[33] Kawahito Y, Mizutani M, Katayama S, Elucidation of high-power fibre laser welding phenomena of stainless steel and effect of factors on weld geometry, J Phys D Appl Phys. 2007; 40.
[34] Molian P.A, Solidification behaviour of laser welded stainless steel, J Mater Sci Lett. 1985; 4: 281-283.
[35] Quan Y.J, Chen Z.H, Gong X.S, Yu Z.H, Effects of heat input on microstructure and tensile properties of laser welded magnesium alloy AZ31, Mater Charact. 2008; 59: 1491-1497.
[36] Mirakhorli F, Malek Ghaini F, Torkamany M.J, Development of weld metal microstructures in pulsed laser welding of duplex stainless steel, J Mater Eng Perform. 2012; 21: 2166-2173.